

Probing Supernovae through gravitational wave entropy

Aknur Sakan^{1,3} , Nurzhan Ussipov^{1,3,*} , Ernazar Abdikamalov^{2,3} , Almat Akhmetali^{1,4} , Marat Zaidyn¹ , Alisher Zhunuskanov¹ , José A. Font^{5,6} , Matthew C. Edwards⁷ , and Sultan Abylkairov^{2,8*} 

¹ Department of Electronics and Astrophysics, Al-Farabi Kazakh National University, 050040 Almaty, Kazakhstan

² Energetic Cosmos Laboratory, Nazarbayev University, 010000 Astana, Kazakhstan

³ Department of Physics, Nazarbayev University, 010000 Astana, Kazakhstan

⁴ Institute of Experimental and Theoretical Physics, 050040 Almaty, Kazakhstan

⁵ Departamento de Astronomía y Astrofísica, Universitat de València, Dr. Moliner 50, 46100 Burjassot (Valencia), Spain

⁶ Observatori Astronòmic, Universitat de València, Catedrático José Beltrán 2, 46980 Paterna, Spain

⁷ Department of Statistics, University of Auckland, Auckland 1010, New Zealand

⁸ School of Artificial Intelligence and Data Science, Astana IT University, 020000 Astana, Kazakhstan

* Correspondence: nurzhan.ussipov@kaznu.edu.kz, sultan.abylkairov@nu.edu.kz

Abstract: We study an entropy-based framework to analyze gravitational-wave signals from core-collapse supernovae. We use waveforms generated by numerical simulations and analyze them in both the time domain and the time-frequency domain using short-time Fourier and continuous wavelet transforms. From each representation, we compute four entropy measures – Shannon, exponential, Rényi, and Tsallis – and apply three feature selection methods to identify the most informative features. We then train machine-learning classifiers on these features to compare the performance of different methodological combinations. We find that the combination of Rényi entropy from the wavelet domain and the Relief-F selection method yields the most effective discrimination among different gravitational-wave signals.

Keywords: core-collapse supernovae, gravitational waves, entropy feature, feature selection

1. Introduction

In 1916, Einstein’s theory of general relativity predicted the existence of gravitational waves, subtle distortions that ripple through the fabric of space-time. They are generated when massive objects accelerate asymmetrically. In 2015, LIGO made the first direct detection of these waves coming from a merger of two black holes [1]. This opened a new window on the universe. Since then, gravitational-wave astronomy has become a key tool for exploring energetic cosmic events such as mergers of black holes and neutron stars [2]. Core-collapse supernovae (CCSNe) are another promising source of GWs [3–5]. Despite decades of study, the exact mechanism behind these explosions remains uncertain [6]. Gravitational waves offer a new way to probe them, carrying information directly from their cores and revealing how massive stars die and compact objects are born [7–9].

Entropy, originally introduced in information theory, quantifies the degree of uncertainty, order, and predictability in a system. It has become a powerful tool for analyzing complex, non-linear, and non-stationary time series data [10]. In gravitational-wave research, entropy-based measures have so far seen limited application, but recent studies have demonstrated their effectiveness for detection [11], classification [12], and for characterizing the complexity and organization of binary-merger signals [13].

Received:

Accepted:

Published:

Citation: Sakan, A.; Ussipov, N.; Abdikamalov, E.; Akhmetali, A.; Zaidyn, M.; Zhunuskanov, A.; Font, J. A.; Edwards, M. C.; Abylkairov, S. Probing supernovae through gravitational wave entropy. *Entropy* **2025**, *1*, 0. <https://doi.org/>

Copyright: © 2025 by the authors. Submitted to *Entropy* for possible open access publication under the terms and conditions of the Creative Commons Attribution (CC BY) license (<https://creativecommons.org/licenses/by/4.0/>).

Entropy could be particularly useful for CCSN gravitational waves, as these signals contain stochastic components arising from turbulent dynamics, superimposed on more coherent features associated with, for example, proto-neutron star oscillations [3,7,14]. By evaluating entropy, one can detect pattern changes and random fluctuations within the signal. These features can then serve as informative inputs for machine-learning algorithms, improving the classification and physical interpretation of CCSN gravitational-wave signals.

In this study, we apply entropy to CCSN gravitational waves. As a first application, we focus on relatively simple signals: the so-called rotating bounce waveforms produced by rapidly rotating progenitors of different masses (more on them in Section 2). The objective is to classify the progenitor mass based on the waveform. These signals are known to be highly similar across masses, making them a challenging test case for machine-learning models [15]. Applying entropy to this problem serves as an intermediate step to assess its utility in a controlled setting. Because rotating bounce signals lack stochastic components, they provide a clean benchmark. More realistic explosions exhibit strong stochasticity due to turbulence [7], which we leave for future work.

With this goal, we perform a systematic machine-learning analysis across multiple signal representations and entropy measures. The analysis is conducted in three domains: the time domain and two time-frequency representations obtained using the short-time Fourier transform and the continuous wavelet transform. We calculate four types of entropy for each representation: Shannon, exponential, Rényi, and Tsallis. We then identify the most informative characteristics using three feature-selection algorithms: Least Absolute Shrinkage and Selection Operator (LASSO), Recursive Feature Elimination with Cross-Validation (RFE-CV), and Relief-F. The selected features are subsequently used to train six machine-learning classifiers, including k -Nearest Neighbors (k -NN), Support Vector Machine (SVM), Random Forest (RF), Logistic Regression (LR), Naïve Bayes (NB), and Extreme Gradient Boosting (XGBoost). The results identify the most informative entropy features, effective feature-selection methods, and classifiers that achieve high accuracy across different signal-to-noise ratios (SNRs).

This paper is organized as follows. Section 2 outlines the astrophysical context of core-collapse supernovae and their gravitational-wave emission. Section 3 describes the computation of entropy features, the feature selection procedures, and the classification algorithms. Section 4 presents the main results, and Section 5 summarizes the key findings and conclusions.

2. Astrophysical Context

For completeness, this section provides additional background on CCSNe and their GW emission. Readers primarily interested in the data analysis and entropy-based methods may skip it without loss of continuity.

Core-collapse supernovae mark the end of massive stars. When such a star exhausts its nuclear fuel, its core can no longer support itself against gravity, and it collapses inward. The collapse stops once matter reaches nuclear densities, creating a rebound that launches a shock wave. This shock quickly loses energy and stalls [16], but if it is revived, it drives a powerful explosion that tears the star apart [17,18]. A successful explosion leaves a neutron star remnant, while failed or partially successful ones may form black holes, either directly or through fallback accretion [19–22].

During collapse, the newborn proto-neutron star emits an enormous number of neutrinos [23,24], and a small fraction of them are absorbed in the region behind the stalled shock [25–27]. This heats the gas, drives turbulent motion, and helps push the shock outward [28–30]. Additional turbulence can also come from large-scale instabilities such

as the standing accretion shock instability [31–33] or from convective plumes originating in the outer stellar layers [34–37]. This mechanism, known as the neutrino mechanism, is believed to power explosions in slowly or non-rotating stars, likely the dominant class among massive stars [38,39].

In rapidly rotating stars, the situation is very different. The forming neutron star gains substantial rotational kinetic energy, which magnetic fields can tap to power the explosion. This mechanism can drive powerful, magnetorotationally driven jet explosions [40–42]. If the jet fails to penetrate the stellar envelope, it can still contribute to the explosion by depositing energy within the star [43,44]. In moderately rotating stars, it is possible that both neutrino heating and magnetic fields contribute to the explosion dynamics [45–49].

Gravitational waves provide a unique means of probing the interior of core-collapse supernovae. Because they originate directly from the stellar core, they carry information about the physical conditions in that region [8,50]. The GW emission mostly arises from oscillations of the proto-neutron star (PNS) [51,52]. Emission from non-radial hydrodynamics instabilities can also contribute [53–57]. Additional, lower-frequency components may result from anisotropic neutrino emission [58,59], asymmetric shock propagation [14,60], or jets [61–63]. When the progenitor rotates rapidly, centrifugal forces distort the collapsing core, so that the proto neutron star formation is accompanied by a sharp gravitational-wave spike at bounce. [64,65]. Rapid rotation can also trigger non-axisymmetric instabilities that produce long-lasting, nearly periodic GW signals [66,67].

Once detected, these signals can provide direct probe of the supernova dynamics [68–70]. They may reveal the mass, radius, and rotation rate of the proto-neutron star [71–74]. Comparing GW patterns across different explosion scenarios could help distinguish between neutrino-driven and magnetorotational supernovae [75,76]. Constraining the properties of high-density nuclear matter is another key objective [77,78], as gravitational-wave observations can help discriminate among competing nuclear models [79–83].

The rich physics of CCSNe makes them interesting laboratories for studying stellar physics and astrophysics under extreme conditions [84–86]. As current and upcoming GW detectors approach the sensitivity to capture these signals [87,88], developing robust methods to characterize and classify them becomes increasingly important. The next sections focus on such methods based on entropy-based representations of GW signals.

3. Methods

This study adopts a probabilistic framework to analyze gravitational-wave signals through four main stages: signal transformation, entropy-based feature extraction, optimal feature selection, and machine learning classification. Each signal representation is converted into a probability distribution, enabling the computation of entropy values. These entropy measures characterize the complexity and structure of the signal. The extracted features are then used to train machine-learning models for classifying gravitational-wave signals from supernovae. The overall workflow of the proposed methodology is illustrated in Figure 1.

3.1. Signal Representation

Signals can be represented in the time, frequency and time-frequency domains. To capture how frequencies change over time, we employ two common time-frequency representations: the short-time Fourier transform (STFT), which uses fixed-size sliding windows, and the continuous wavelet transform (CWT), which uses scale-dependent sliding windows to achieve higher time resolution at high frequencies and higher frequency resolution at low frequencies. To quantify local variations in signal complexity, the signal is divided

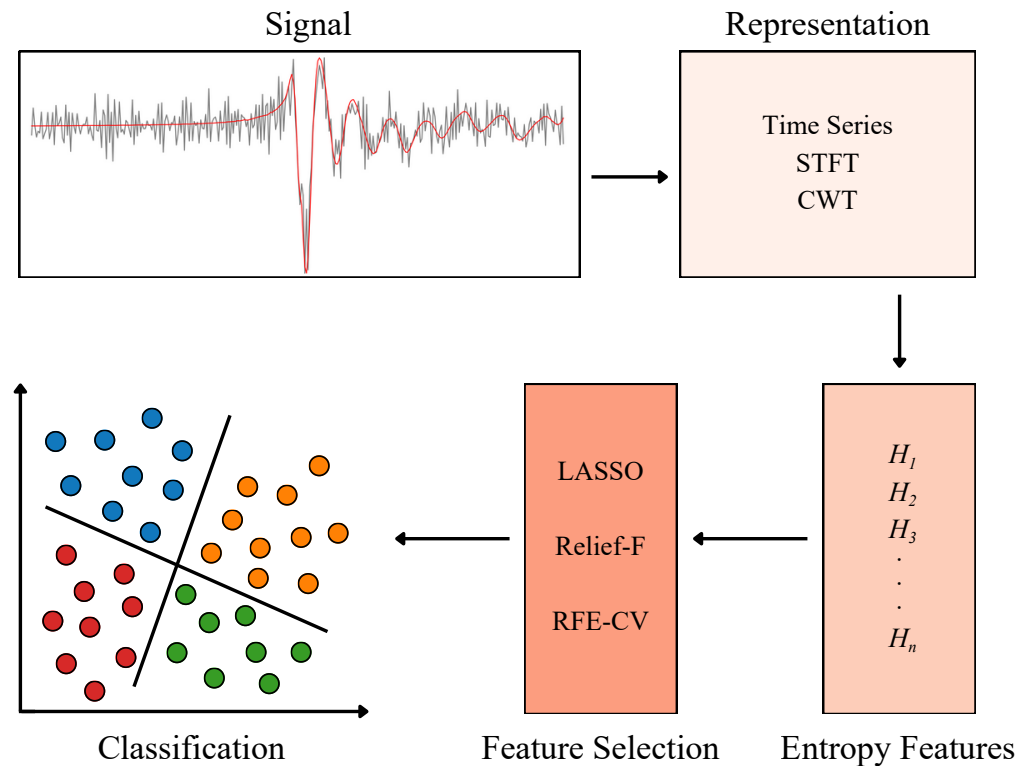


Figure 1. Flowchart outlining the main steps of the proposed methodology. The signal representation stage (Time series, STFT, CWT) is described in Section 3.1, the entropy feature extraction in Section 3.2, the feature selection methods (LASSO, Relief-F, RFE-CV) and the classification procedure in Section 3.3.

into segments, and a probability distribution is computed for each segment. Here, the segment length is set to 10% of the total signal duration.

To characterize the statistical properties of the gravitational wave strain signal, we construct a probability distribution from the time-domain strain data of a single waveform. The strain values, which range from h_{min} to h_{max} , are partitioned into discrete bins of width Δh . For each bin k , we count the number of data points N_k whose strain values fall within that bin's range. The probability distribution is then obtained by normalizing these counts:

$$p_k = \frac{N_k}{\sum_k N_k}, \quad (1)$$

where N_k is the number of data points in the k -th bin and $\sum_k N_k$ is the total number of data points in the waveform. This distribution characterizes the relative frequency with which different strain values occur throughout the gravitational wave signal.

The STFT decomposes a segment into localized frequency components by applying a window function [89,90]. The STFT coefficients are given by

$$X(f, t) = \sum_n x[n] g[n - t] e^{-j2\pi f n / M}, \quad (2)$$

where $g(\cdot)$ denotes the analysis window and j is the imaginary unit. The STFT was computed using a Hann window of length 256 samples, with consecutive segments overlapping by 50%. The complex magnitudes are then normalized to form a probability distribution:

$$p_{f,t} = \frac{|X(f, t)|}{\sum_f \sum_t |X(f, t)|}. \quad (3)$$

The CWT provides simultaneous localization in both the time and frequency domains [91,92]. For a segment, the CWT is defined as

$$W_x(s, \tau) = \frac{1}{\sqrt{s}} \int_{-\infty}^{\infty} x(t) \psi^* \left(\frac{t - \tau}{s} \right) dt, \quad (4)$$

where ψ is the mother wavelet, s denotes scale. The CWT was computed using the Mexican Hat wavelet with a frequency range of 50-2000 Hz.

The magnitudes are normalized to form a probability distribution:

$$p_{s,\tau} = \frac{|W_x(s, \tau)|}{\sum_s \sum_{\tau} |W_x(s, \tau)|}. \quad (5)$$

These normalized distributions all satisfy $\sum p = 1$, making them suitable for entropy-based measures of signal complexity.

3.2. Entropy Feature Extraction

Entropy measures provide a quantitative description of the uncertainty or information content inherent in a probability distribution. In this study, several entropy-based metrics are used as features to characterize the statistical complexity of the signals.

Shannon entropy quantifies the average uncertainty in a probabilistic event [93] and is defined as follows:

$$H_{\text{Sh}} = - \sum_{i=1}^M p_i \log_2 p_i, \quad (6)$$

where M is the number of bins.

Exponential entropy replaces the logarithmic dependence of Shannon entropy with an exponential mapping [94]:

$$H_{\text{Exp}}(X) = \sum_{i=1}^M (1 - e^{-p_i}). \quad (7)$$

The main advantage of this method is that it emphasizes rare events. This form matches the implementation used in the analysis and increases monotonically with p_i .

Tsallis entropy introduces a real-valued entropic index q , which controls the degree of nonadditivity and sensitivity to correlations in the data [95]. It is computed as :

$$H_q(X) = \frac{1 - \sum_{i=1}^M p_i^q}{q - 1}. \quad (8)$$

When $q \rightarrow 1$, Tsallis entropy converges to the Shannon entropy.

Rényi entropy generalizes Shannon entropy through an order parameter α , controlling how probabilities are weighted [96]. It is computed as follows :

$$H_{\alpha}^{(\text{R})}(X) = \frac{\log_2 \left(\sum_{i=1}^M p_i^{\alpha} \right)}{1 - \alpha}. \quad (9)$$

The base-2 logarithm ensures consistency with the Shannon definition. As $\alpha \rightarrow 1$, Rényi entropy approaches the normalized Shannon entropy.

3.3. Feature Selection

Feature selection identifies the most informative variables while removing redundant or noisy ones, thus reducing overfitting, lowering computational cost, and improving model interpretability [97,98]. In this work, we employ three representative algorithms: LASSO, RFE-CV, and the Relief-F algorithm. LASSO applies an L_1 regularization penalty to

Table 1. Grid of hyperparameters used for tuning classical ML models. The optimal hyperparameters are highlighted in bold.

Random Forest	Support Vector Machines	Naïve Bayes
<code>'n_estimators': [50, 75, 100, 125, 150]</code> <code>'max_depth': [None, 10, 15, 20]</code> <code>'min_samples_split': [2, 5, 10]</code> <code>'min_samples_leaf': [1, 2, 4]</code>	<code>'C': [0.1, 1, 10]</code> <code>'kernel': ['linear', 'rbf', 'poly']</code> <code>'gamma': [scale, 'auto']</code> <code>'degree': [2, 3, 4]</code>	<code>'var_smoothing': [10⁻⁹, 10⁻⁸, 10⁻⁷, 10⁻⁶, 10⁻⁵]</code>
Logistic Regression	<i>k</i> -Nearest Neighbors	eXtreme Gradient Boosting
<code>'C': [0.01, 0.1, 1, 10, 100]</code> <code>'penalty': ['l1', 'l2', 'none']</code> <code>'solver': ['lbfgs', 'liblinear', 'saga']</code> <code>'max_iter': [100, 200, 300]</code>	<code>'n_neighbors': [3, 5, 7, 9, 11]</code> <code>'weights': ['uniform', distance]</code> <code>'metric': ['euclidean', 'manhattan', 'minkowski']</code> <code>'p': [1, 2]</code>	<code>'n_estimators': [50, 100, 200]</code> <code>'max_depth': [3, 5, 7]</code> <code>'learning_rate': [0.01, 0.1, 0.2]</code> <code>'subsample': [0.8, 0.9, 1.0]</code> <code>'colsample_bytree': [0.8, 0.9, 1.0]</code> <code>'gamma': [0, 0.1, 0.2]</code> <code>'reg_alpha': [0, 0.01, 0.1]</code> <code>'reg_lambda': [1, 0.1, 0.01]</code>

suppress irrelevant coefficients and produce sparse, interpretable models [99–101]. RFE-CV iteratively eliminates the least relevant features while optimizing performance through cross-validation [102]. Relief-F, a distance-based approach, evaluates features by their ability to distinguish neighboring samples from different classes, providing robustness against noise and missing data [103,104].

3.4. Classification

After feature selection, we use six classical machine learning (ML) algorithms for classification. To ensure optimal and fair performance across models, each classifier is tuned using `GridSearchCV` with 5-fold cross-validation [105]. In this procedure, the dataset is divided into five folds. For every combination of hyperparameters, the model is trained on four folds and validated on the remaining one. This process repeats until each fold has served as a validation set and the average classification accuracy across all folds is computed to evaluate model performance. The combination of hyperparameters that yields the highest average accuracy is selected as optimal.

To verify that the tuned models generalize well, the mean accuracy on the training folds is compared with that on validation folds. The absence of a significant performance gap indicates that the models are neither overfitting nor underfitting. The resulting optimal hyperparameters for each model are summarized in Table 1, where the best configurations obtained through `GridSearchCV` are highlighted in bold.

After determining the optimal hyperparameters, the dataset is split into training and test sets with an 80:20 ratio. Model performance is evaluated based on accuracy, which quantifies the proportion of correctly predicted samples relative to the total number of predictions, defined as:

$$\text{Accuracy} = \frac{\text{Number of Correct Predictions}}{\text{Total Number of Predictions}}. \quad (10)$$

This evaluation ensures a fair and consistent comparison of all ML models under the same data and noise conditions.

3.5. Dataset

The dataset was obtained from numerical simulations using the general relativistic CoCoNuT code [106,107] for progenitor models with zero-age main sequence (ZAMS) masses of 12, 15, 27, and 40 Solar mass. The $12 M_{\odot}$ and $40 M_{\odot}$ progenitor models were developed by Woosley and Heger [108], the $15 M_{\odot}$ model by Heger et al. [38], and the $27 M_{\odot}$ model

by Woosley et al. [109]. All progenitor models assume solar metallicity. For each progenitor mass, six equations of state (EOS): SFHo, SFHx, GShenFSU2.1, HSDD2, LS220, and BHB Λ Φ, were selected from the Richers et al. [77] catalog based on their consistency with current observational constraints. For each EOS, we simulated a number of rotational configurations, the number ranging from 52 to 56. We quantify the impact of rotation by the ratio $T/|W|$, where T denotes rotational kinetic energy and W denotes gravitational binding energy. The number of rotation configurations varies because some EOS models do not undergo core collapse within the given simulation time limit. We consider $T/|W|$ values ranging from 0.02 to 0.21. This yields 1332 unique gravitational waveforms in total. All waveform data have a sampling rate of 16384 Hz, which matches LIGO's operational sampling rate. The upper limit for the simulated signals is imposed by code limitations in accurately modeling post-bounce dynamics beyond \sim 6–8 ms after the bounce time ($t = 0$).

To qualify the noise level presented in the signal we use signal-to-noise ratio [110], the matched-filter SNR ρ for a detected GW signal h is defined under the assumption of a perfectly matched template,

$$\rho = \sqrt{\int_0^\infty \frac{4\hat{h}^*(f)\hat{h}(f)}{S_n(f)} df}, \quad (11)$$

where $\hat{h}(f)$ is the Fourier transform of the template waveform and $S_n(f)$ is the one-sided noise spectral density. All SNR values are calculated assuming optimal orientation of both the detector and the source. In this work, we use the Advanced LIGO noise spectrum at its design sensitivity, specifically in the high-power, zero-detuning configuration. Figure 2 shows example waveforms for SFHo EOS and $T/|W| = 0.07$.

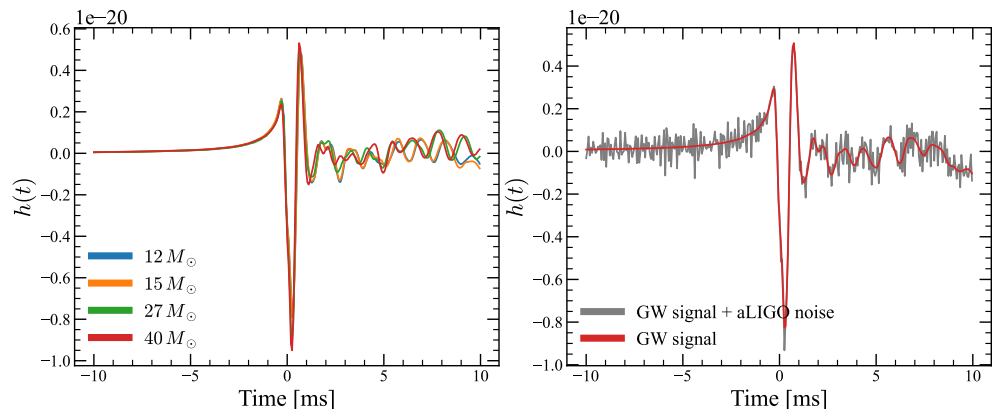


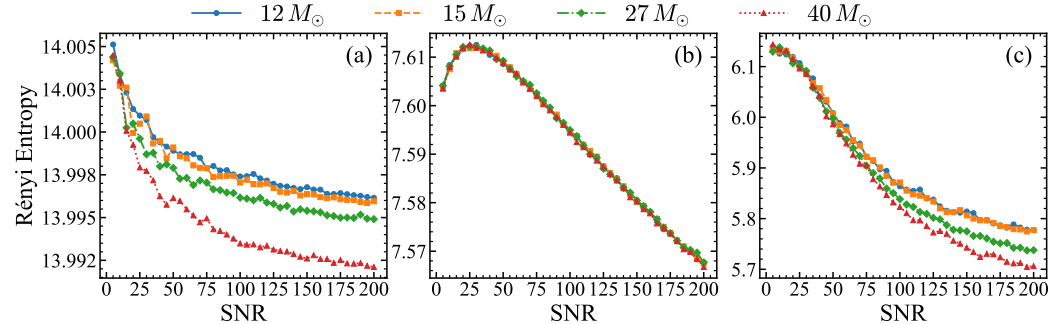
Figure 2. Gravitational wave strain as a function of time. Left: clean signals generated for four different source masses. Right: example of a single signal for the SFHo EOS with $T/|W| = 0.07$ and a $40 M_\odot$ mass after the addition of noise corresponding to an SNR of 200.

4. Results

In this section, we evaluate how different representations, entropy types, feature selection algorithms, and classification methods affect accuracy. Our goal is to identify the optimal combination that most effectively distinguishes between different masses of GW sources. We start from a default model setup that combines the CWT representation, Rényi entropy with $\alpha = 2$, Relief-F feature selection, and an SVM classifier (see Table 2). We then vary each element in this setup to examine how it affects classification accuracy.

Table 2. Parameters of the default model configuration used for performance assessment.

Parameter	Default choice
Signal representation	CWT
Entropy feature	Rényi entropy ($\alpha = 2$)
Feature selection	Relief-F
Classifier	SVM

**Figure 3.** Rényi entropy ($\alpha = 2$) as a function of SNR for CWT (a), STFT (b), and time series representations (c).

4.1. Dependence on representation

In this section, we evaluate which representation – time series, STFT, or CWT – provides the most informative characterization of GW signals. To this end, we compute entropy values and classification accuracies for all three representations using the default model configuration summarized in Table 2.

In Figure 3, the average Rényi entropy ($\alpha = 2$) as a function of SNR for the three signal representations: CWT, STFT, and time series. Among them, the CWT representation provides the clearest visual separation between different mass classes across the SNR range, suggesting that it preserves more discriminative information under varying noise levels. The time series representation shows moderate class distinction, while the STFT-based entropy exhibits no clear separation between masses. This is likely because the STFT uses a fixed time-frequency resolution, which limits its ability to capture the nonstationary and transient features characteristic of GW signals. In contrast, the CWT adapts its resolution across frequencies, retaining both low- and high-frequency components that vary with progenitor mass. Overall, the CWT representation shows the most stable and consistent entropy behavior, making it the most suitable representation for subsequent classification.

Note that the STFT-based entropy displays a characteristic peak at SNR of about 25. At lower values of SNR, entropy increases due to the stronger influence of noise on the spectral components. This behavior arises from the fixed time-frequency resolution of the STFT, which causes noise to be distributed uniformly within each analysis window, increasing uncertainty in the spectral energy distribution. As SNR increases, noise effects

Table 3. Classification accuracy of the SVM (mean \pm std) for different entropy measures obtained using various signal representations at SNR = 200.

Entropy type	CWT	STFT	Time Series
Shannon	0.733 ± 0.025	0.391 ± 0.026	0.316 ± 0.028
Exponential	0.731 ± 0.027	0.410 ± 0.026	0.319 ± 0.025
Rényi, $\alpha = 2$	0.740 ± 0.027	0.410 ± 0.027	0.316 ± 0.025
Tsallis, $q = 1.5$	0.737 ± 0.023	0.400 ± 0.028	0.319 ± 0.022

diminish, the signal structure becomes more pronounced, and entropy gradually decreases, reflecting a transition from a stochastic to a deterministic regime.

To complement these findings, Table 3 reports the classification accuracies obtained using different entropy measures derived from CWT, STFT, and time series representations. The CWT consistently achieves the highest accuracy, exceeding ~ 0.7 . In contrast, STFT and time series representations yield noticeably lower accuracies, remaining below ~ 0.41 . These results confirm that entropy features computed from the CWT provide a more discriminative and informative representation for signal classification compared to STFT and time-domain forms.

4.2. Dependence on entropy

We investigate how varying the type of entropy measure impacts classification accuracy. All remaining parameters are held at their default values (Table 2).

Figure 4 shows the values of the four entropy measures as a function of SNR. In all cases, entropy decreases with increasing SNR, as the noise contribution diminishes and the signal structure becomes more ordered. Beyond a certain SNR threshold, further changes in entropy are mainly governed by the intrinsic randomness of the signal rather than external noise. Overall, different types of entropy measures yield qualitatively similar results.

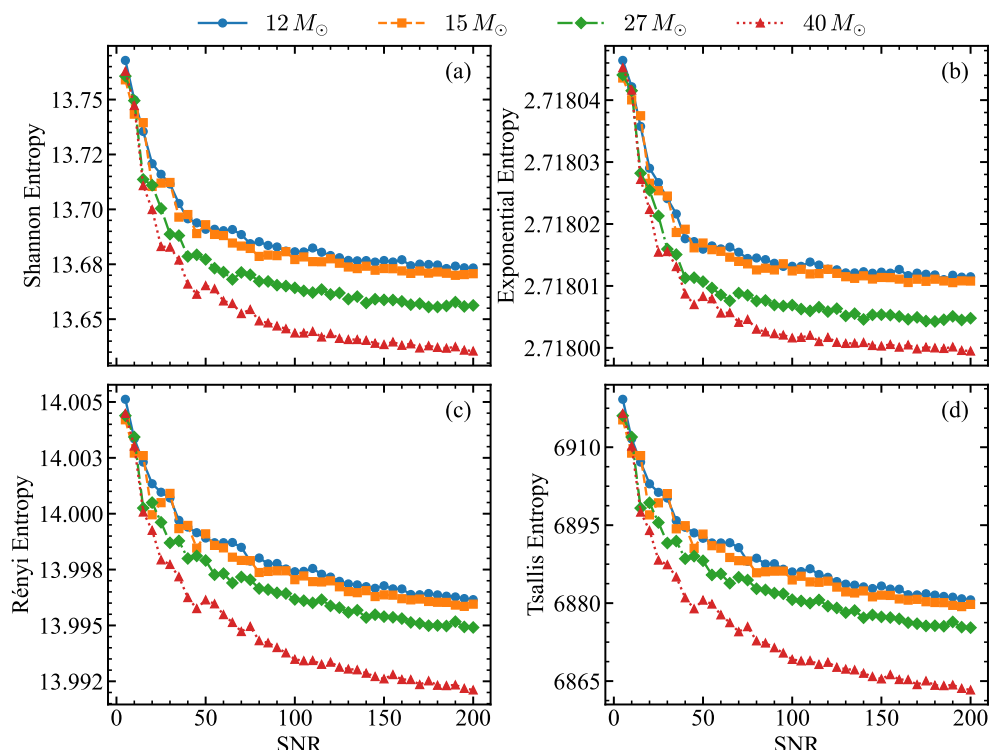


Figure 4. Various types of entropy as a function of SNR estimated with CWT. (a) Shannon entropy; (b) Exponential entropy; (c) Rényi entropy; (d) Tsallis entropy.

These results also shed light on the dependence of entropy measures on the source mass: higher-mass progenitors yield lower entropy values, indicating greater signal regularity. While all four entropy features distinguish most signal classes ($12, 27$, and $40 M_{\odot}$) at high SNRs, partial overlap remains between the $12 M_{\odot}$ and $15 M_{\odot}$ cases due to their spectral similarity and smaller relative differences. This is true across all types of entropy measures.

In Table 3, we summarize the values of the classification accuracy for different types of entropy measures. Close inspection of these values support the trend noticed above:

the choice of entropy type has only a minor impact on classification accuracy, with values ranging from 0.731 ± 0.027 to 0.740 ± 0.037 . The highest accuracy is achieved using Rényi entropy with $\alpha = 2$.

In Figure 5, we show how the classification accuracy depends on the parameters α and q of the Rényi and Tsallis entropies, respectively. For Rényi entropy, accuracy increases steadily with α up to a maximum at $\alpha = 2$, after which it gradually declines. A similar trend is observed for Tsallis entropy, which reaches its peak accuracy at $q = 1.5$.

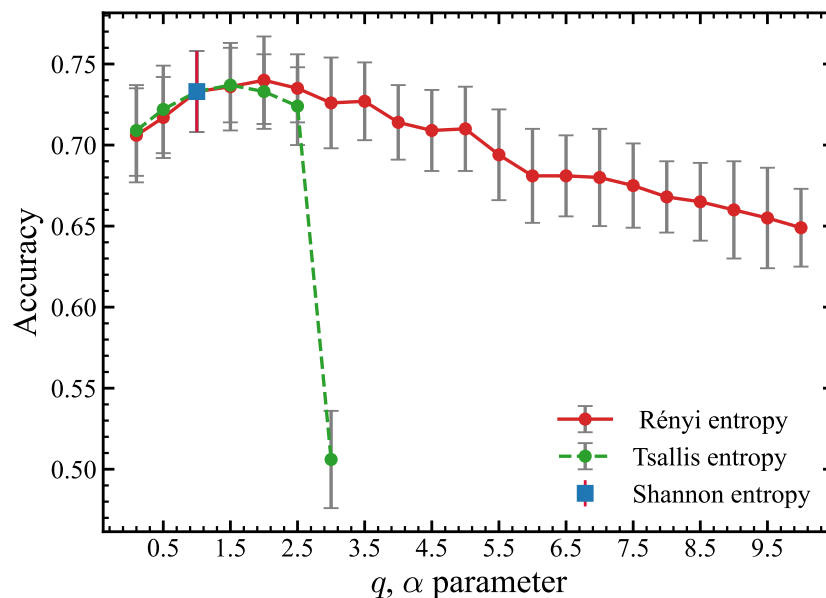


Figure 5. Dependence of accuracy on α and q parameters of Rényi and Tsallis entropy at SNR = 200. The remaining parameters correspond to those of the optimal model configuration (Table 2). For $q = 1$ and $\alpha = 1$, both Rényi and Tsallis entropies reduce to the Shannon entropy, highlighted by the blue square.

4.3. Dependence on feature selection

In this section, we examine how different feature selection methods influence classification accuracy. All model parameters, except the feature selection methods, are kept at their default values (Table 2).

Table 4 presents the results for various feature selection strategies. The overall performance without feature selection shows that applying LASSO and RFE-CV leads to only minor changes in accuracy, indicating that these methods neither substantially improve nor reduce the effectiveness of the entropy-based features.

In contrast, the Relief-F method led to a modest improvement, achieving the highest overall accuracy among all tested methods. This suggests that Relief-F can provide a slightly more refined and discriminative subset of entropy features, thereby improving the model's ability to distinguish between different GW source classes.

4.4. Dependence on classification algorithm

In this section, we examine how different classification models affect the classification accuracy. All model parameters, except the classification algorithms, are kept at their default values (Table 2).

As shown in Table 4, the SVM achieves the highest accuracy among all classifiers, reaching 77.4% in the default configuration. This result highlights its effectiveness in

Table 4. Classification accuracy (mean \pm std) of different classifiers for the original feature set and after applying various feature selection (FS) methods at SNR = 200 using CWT and Rényi entropy with $\alpha = 2$.

Name of classifier	No FS	LASSO FS	RFE-CV FS	Relief-F FS
SVM	0.740 ± 0.027	0.731 ± 0.026	0.736 ± 0.028	0.774 ± 0.025
<i>k</i> -NN	0.639 ± 0.026	0.656 ± 0.029	0.632 ± 0.025	0.658 ± 0.027
XGB	0.595 ± 0.026	0.606 ± 0.029	0.594 ± 0.028	0.634 ± 0.028
Random Forest	0.604 ± 0.030	0.611 ± 0.030	0.591 ± 0.028	0.645 ± 0.030
Naïve Bayes	0.365 ± 0.032	0.390 ± 0.031	0.399 ± 0.028	0.397 ± 0.031
Logistic Regression	0.411 ± 0.025	0.431 ± 0.027	0.437 ± 0.027	0.428 ± 0.030

handling entropy-based features and capturing complex, nonlinear relationships within the data. For additional results from STFT and time series, we refer readers to Tables A5 and A6 in Appendix A.

4.5. Optimal configuration

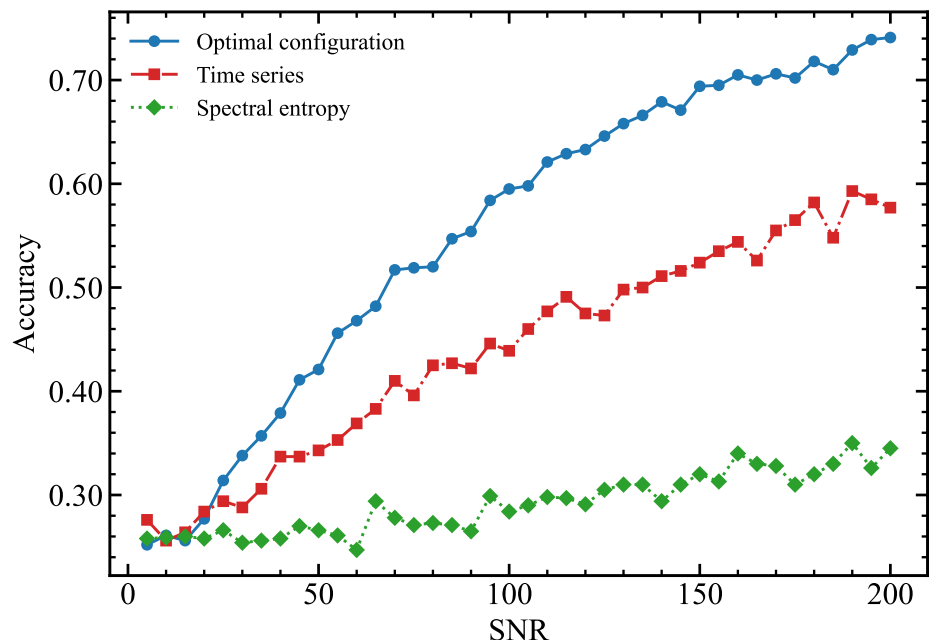


Figure 6. Classification accuracy as a function of SNR for the optimal configuration (blue line), raw time series data (red line) and spectral entropy (green line).

The previous results indicate that the most effective configuration consists of the CWT as the signal representation (Figure 3, Table 3), Rényi entropy with parameter $\alpha = 2$ as the entropy feature (Table 3), Relief-F as the feature selection method (Table 4), and SVM as the classification algorithm (Table 4). This combination provides the highest classification accuracy and the most stable performance across varying SNR levels. Below, we analyze how this accuracy depends on SNR. In addition, we add a comparison with traditional classification approaches that rely on raw time-series data and spectral entropy. Spectral entropy, calculated from the Fourier power spectrum, is used here as a baseline since it is a widely adopted Shannon-based measure of signal complexity that reflects the degree of spectral disorder [111–113].

Figure 6 shows the mean classification accuracy as a function of SNR for the optimal configuration identified in this work, compared with results from raw time-series data and

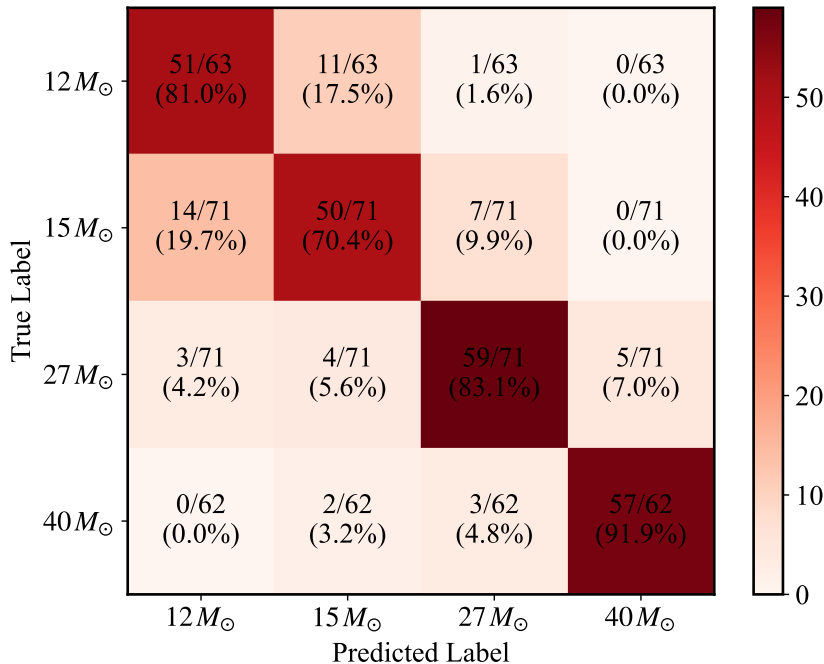


Figure 7. Confusion matrix for optimal model configuration for SNR=200. The parameters of the optimal model configuration is given in Table 2.

spectral entropy. The proposed configuration consistently achieves higher accuracy across all SNR levels.

Figure 7 shows the SVM confusion matrix for the optimal configuration at SNR = 200. The results indicate strong classification performance across all four progenitor mass classes, with particularly high accuracy for the 40 and 27 M_{\odot} models. Some overlap is observed between the 12 and 15 M_{\odot} classes due to the similarity of their waveform morphologies.

5. Conclusions

In this work, we studied entropy-based feature for classifying gravitational waves from core-collapse supernovae. We focus on rotating bounce signal for progenitors with four different masses and six equations of state. We compute entropy measures from time series, STFT, and CWT representations. To identify the most informative characteristics, three feature-selection algorithms, including LASSO, RFE-CV, and Relief-F were applied in combination with six machine-learning classifiers.

The results show that wavelet-based entropy features yield the highest classification accuracy, exceeding $\sim 70\%$ for our gravitational-wave signals. In contrast, the accuracies obtained from the time-series and STFT representations remain below $\sim 40\%$. This confirms that time-frequency representations encode richer discriminative information than purely temporal or spectral analyses. Different entropy measures produce comparable outcomes; however, among all tested measures, Rényi entropy with $\alpha = 2$ derived from the CWT achieves the highest accuracy.

Feature selection also influences classification performance. While LASSO and RFE-CV provided only modest improvements, the Relief-F algorithm delivered the best overall result. Among classifiers, the SVM yields the highest accuracy. Overall, the combination of CWT-based Rényi entropy and Relief-F feature selection yields the best performance with classification accuracy of $\sim 77\%$.

These results suggest that entropy-based methods hold promise for studying gravitational-wave signals from core-collapse supernovae. Nevertheless, our study has several limitations. Our analysis focuses on rotating bounce signals, which are relatively

easy to model and detect but likely rare in nature, and they lack stochastic components. In future work, we plan to extend the analysis to more realistic signals that include stochastic features arising from turbulent dynamics. In addition, the optimal method configuration identified here is based on waveforms from different progenitor masses, and its applicability to other tasks (e.g., measurement of rotation or equation-of-state) remains to be tested. We also assume an optimal source orientation, whereas real sources have random orientations. Finally, detector noise is modeled as simulated Gaussian noise, which represents a simplified approximation to realistic instrumental noise. These limitations will be systematically addressed in future studies.

Appendix A Additional results

This appendix provides supplementary classification results obtained using the STFT and time-series representations.

Table A5. Classification accuracy (mean \pm std) of different classifiers for the original feature set and after applying various feature selection (FS) methods at SNR = 200 using STFT transform.

Name of classifier	No FS	LASSO FS	RFE-CV FS	Relief-F FS
SVM	0.410 ± 0.025	0.404 ± 0.027	0.410 ± 0.028	0.438 ± 0.026
<i>k</i> -NN	0.356 ± 0.027	0.378 ± 0.028	0.358 ± 0.027	0.406 ± 0.024
XGB	0.397 ± 0.030	0.402 ± 0.027	0.384 ± 0.027	0.410 ± 0.026
Random Forest	0.389 ± 0.027	0.404 ± 0.030	0.390 ± 0.027	0.395 ± 0.026
Naïve Bayes	0.355 ± 0.026	0.370 ± 0.027	0.380 ± 0.030	0.364 ± 0.028
Logistic Regression	0.352 ± 0.026	0.374 ± 0.027	0.395 ± 0.030	0.359 ± 0.027

Table A6. Classification accuracy (mean \pm std) of different classifiers for the original feature set and after applying various feature selection (FS) methods at SNR = 200 using time series.

Name of Classifiers	No FS	LASSO FS	RFE-CV FS	Relief-F FS
SVM	0.313 ± 0.025	0.322 ± 0.025	0.331 ± 0.025	0.329 ± 0.028
<i>k</i> -NN	0.280 ± 0.025	0.279 ± 0.023	0.289 ± 0.026	0.297 ± 0.028
XGB	0.313 ± 0.027	0.318 ± 0.027	0.325 ± 0.022	0.324 ± 0.026
Random Forest	0.318 ± 0.029	0.332 ± 0.026	0.338 ± 0.028	0.330 ± 0.028
Naïve Bayes	0.296 ± 0.024	0.308 ± 0.023	0.322 ± 0.024	0.308 ± 0.026
Logistic Regression	0.324 ± 0.025	0.348 ± 0.026	0.356 ± 0.025	0.332 ± 0.026

Author Contributions: Conceptualization, N.U. and A.S.; methodology, A.A. ; software, M.Z.; validation, and formal analysis, A.S.; investigation, A.Z.; resources, A.A.; data curation, S.A.; writing-original draft preparation, A.S.; writing-review and editing, E.A., A.A., J.A.F and M.C.E.; visualization, A.Z.; supervision, E.A and N.U.; project administration, N.U.; funding acquisition, E.A. All authors have read and agreed to the published version of the manuscript.

Funding: This research was funded by the Science Committee of the Ministry of Science and Higher Education of the Republic of Kazakhstan (Grant No. AP26103591) and partially supported by the Nazarbayev University Faculty Development Competitive Research Grant Program (no. 040225FD4713). JAF is funded by the Spanish Agencia Estatal de Investigación (grant PID2024-159689NB-C21) and by the Generalitat Valenciana (Prometeo excellence programme grant CIPROM/2022/49).

Data Availability Statement: The raw data supporting the conclusions of this article will be made available by the authors on request.

Conflicts of Interest: The authors declare no conflicts of interest.

References

1. Abbott, B.P.; et al. Observation of gravitational waves from a binary black hole merger. *Phys. Rev. Lett.* **2016**, *116*, 061102. <https://doi.org/10.1103/PhysRevLett.116.061102>.
2. The LIGO Scientific Collaboration.; the Virgo Collaboration.; the KAGRA Collaboration.; Abac, A.G.; Abouelfettouh, I.; Acernese, F.; Ackley, K.e.a. GWTC-4.0: Updating the Gravitational-Wave Transient Catalog with Observations from the First Part of the Fourth LIGO-Virgo-KAGRA Observing Run. *arXiv e-prints* **2025**, p. arXiv:2508.18082, [arXiv:gr-qc/2508.18082]. <https://doi.org/10.48550/arXiv.2508.18082>.
3. Müller, B.; Janka, H.T.; Marek, A. A New Multi-dimensional General Relativistic Neutrino Hydrodynamics Code of Core-collapse Supernovae. III. Gravitational Wave Signals from Supernova Explosion Models. *Astrophys. J.* **2013**, *766*, 43, [arXiv:astro-ph.SR/1210.6984]. <https://doi.org/10.1088/0004-637X/766/1/43>.
4. Abbott, B.P.; et al. Optically targeted search for gravitational waves emitted by core-collapse supernovae during the first and second observing runs of advanced LIGO and advanced Virgo. *Phys. Rev. D* **2020**, *101*, 084002. <https://doi.org/10.1103/PhysRevD.101.084002>.
5. Kotake, K.; Kuroda, T. Gravitational Waves from Core-Collapse Supernovae. In *Handbook of Supernovae*; Alsabti, A.W.; Murdin, P., Eds.; 2017; p. 1671. https://doi.org/10.1007/978-3-319-21846-5_9.
6. Müller, B. Hydrodynamics of core-collapse supernovae and their progenitors. *Living Reviews in Computational Astrophysics* **2020**, *6*, 3, [arXiv:astro-ph.SR/2006.05083]. <https://doi.org/10.1007/s41115-020-0008-5>.
7. Abdikamalov, E.; Pagliaroli, G.; Radice, D. Gravitational Waves from Core-Collapse Supernovae. In *Handbook of Gravitational Wave Astronomy*; Bambi, C.; Katsanevas, S.; Kokkotas, K.D., Eds.; 2022; p. 21. https://doi.org/10.1007/978-981-15-4702-7_21-1.
8. Mezzacappa, A.; Zanolin, M. Gravitational Waves from Neutrino-Driven Core Collapse Supernovae: Predictions, Detection, and Parameter Estimation. *arXiv e-prints* **2024**, p. arXiv:2401.11635, [arXiv:astro-ph.HE/2401.11635]. <https://doi.org/10.48550/arXiv.2401.11635>.
9. Szczepańczyk, M.J.; et al. Optically targeted search for gravitational waves emitted by core-collapse supernovae during the third observing run of Advanced LIGO and Advanced Virgo. *Phys. Rev. D* **2024**, *110*, 042007. <https://doi.org/10.1103/PhysRevD.110.042007>.
10. Sepúlveda-Fontaine, S.A.; Amigó, J.M. Applications of Entropy in Data Analysis and Machine Learning: A Review. *Entropy* **2024**, *26*, 1126, [arXiv:stat.ML/2503.02921]. <https://doi.org/10.3390/e26121126>.
11. Zhanabaev, Z.; Ussipov, N. INFORMATION-ENTROPY METHOD FOR DETECTING GRAVITATIONAL WAVE SIGNALS. *Eurasian Physical Technical Journal* **2023**, *20*, 79–86. <https://doi.org/10.31489/2023NO2/79-86>.
12. Ussipov, N.; Zhanabaev, Z.; Akhmetali, A.; Zaidyn, M.; Turlykzhanayeva, D.; Akniyazova, A.; Namazbayev, T. Classification of Gravitational Waves from Black Hole-Neutron Star Mergers with Machine Learning. *Journal of Astronomy and Space Sciences* **2024**, *41*, 149–158. <https://doi.org/10.5140/JASS.2024.41.3.149>.
13. Javaherian, M.; Mollaei, S. Multiscale Entropy Analysis of Gravitational Waves. *Advances in High Energy Physics* **2021**, *2021*, 6643546, [<https://onlinelibrary.wiley.com/doi/pdf/10.1155/2021/6643546>]. <https://doi.org/https://doi.org/10.1155/2021/6643546>.
14. Radice, D.; Morozova, V.; Burrows, A.; Vartanyan, D.; Nagakura, H. Characterizing the Gravitational Wave Signal from Core-collapse Supernovae. *Astrophys. J. Lett.* **2019**, *876*, L9, [arXiv:astro-ph.HE/1812.07703]. <https://doi.org/10.3847/2041-8213/ab191a>.
15. Mitra, A.; Shukirgaliyev, B.; Abylkairov, Y.S.; Abdikamalov, E. Exploring supernova gravitational waves with machine learning. *MNRAS* **2023**, *520*, 2473–2483, [arXiv:astro-ph.HE/2209.14542]. <https://doi.org/10.1093/mnras/stad169>.
16. Liebendörfer, M.; Mezzacappa, A.; Thielemann, F.K.; Messer, O.E.; Hix, W.R.; Bruenn, S.W. Probing the gravitational well: No supernova explosion in spherical symmetry with general relativistic Boltzmann neutrino transport. *Phys. Rev. D* **2001**, *63*, 103004, [arXiv:astro-ph/astro-ph/0006418]. <https://doi.org/10.1103/PhysRevD.63.103004>.
17. Burrows, A.; Gosh, J. A Theory of Supernova Explosions. *Astrophys. J. Lett.* **1993**, *416*, L75. <https://doi.org/10.1086/187074>.
18. Janka, H.T. Conditions for shock revival by neutrino heating in core-collapse supernovae. *A&A* **2001**, *368*, 527–560, [arXiv:astro-ph/astro-ph/0008432]. <https://doi.org/10.1051/0004-6361:20010012>.
19. Kuroda, T.; Fischer, T.; Takiwaki, T.; Kotake, K. Core-collapse Supernova Simulations and the Formation of Neutron Stars, Hybrid Stars, and Black Holes. *Astrophys. J.* **2022**, *924*, 38, [arXiv:astro-ph.HE/2109.01508]. <https://doi.org/10.3847/1538-4357/ac31a8>.
20. Burrows, A.; Vartanyan, D.; Wang, T. Black Hole Formation Accompanied by the Supernova Explosion of a $40 M_{\odot}$ Progenitor Star. *Astrophys. J.* **2023**, *957*, 68, [arXiv:astro-ph.SR/2308.05798]. <https://doi.org/10.3847/1538-4357/acfc1c>.
21. Powell, J.; Müller, B. Gravitational waves from core-collapse supernovae with no electromagnetic counterparts. *arXiv e-prints* **2025**, p. arXiv:2506.03581, [arXiv:astro-ph.HE/2506.03581]. <https://doi.org/10.48550/arXiv.2506.03581>.
22. Eggenberger Andersen, O.; O'Connor, E.; Andresen, H.; da Silva Schneider, A.; Couch, S.M. Black Hole Supernovae, Their Equation of State Dependence, and Ejecta Composition. *Astrophys. J.* **2025**, *980*, 53, [arXiv:astro-ph.HE/2411.11969]. <https://doi.org/10.3847/1538-4357/ada899>.

23. Rampp, M.; Janka, H.T. Spherically Symmetric Simulation with Boltzmann Neutrino Transport of Core Collapse and Postbounce Evolution of a 15 M_{solar} Star. *Astrophys. J. Lett.* **2000**, *539*, L33–L36, [[arXiv:astro-ph/astro-ph/0005438](#)]. <https://doi.org/10.1086/312837>.

24. O'Connor, E.; Ott, C.D. The Progenitor Dependence of the Pre-explosion Neutrino Emission in Core-collapse Supernovae. *Astrophys. J.* **2013**, *762*, 126, [[arXiv:astro-ph.HE/1207.1100](#)]. <https://doi.org/10.1088/0004-637X/762/2/126>.

25. Buras, R.; Janka, H.T.; Rampp, M.; Kifonidis, K. Two-dimensional hydrodynamic core-collapse supernova simulations with spectral neutrino transport. II. Models for different progenitor stars. *A&A* **2006**, *457*, 281–308, [[arXiv:astro-ph/astro-ph/0512189](#)]. <https://doi.org/10.1051/0004-6361:20054654>.

26. Bruenn, S.W.; Lentz, E.J.; Hix, W.R.; Mezzacappa, A.; Harris, J.A.; Messer, O.E.B.; Endeve, E.; Blondin, J.M.; Chertkow, M.A.; Lingerfelt, E.J.; et al. The Development of Explosions in Axisymmetric Ab Initio Core-collapse Supernova Simulations of 12–25 M Stars. *Astrophys. J.* **2016**, *818*, 123, [[arXiv:astro-ph.SR/1409.5779](#)]. <https://doi.org/10.3847/0004-637X/818/2/123>.

27. Kotake, K.; Takiwaki, T.; Fischer, T.; Nakamura, K.; Martínez-Pinedo, G. Impact of Neutrino Opacities on Core-collapse Supernova Simulations. *Astrophys. J.* **2018**, *853*, 170, [[arXiv:astro-ph.HE/1801.02703](#)]. <https://doi.org/10.3847/1538-4357/aaa716>.

28. Abdikamalov, E.; Ott, C.D.; Radice, D.; Roberts, L.F.; Haas, R.; Reisswig, C.; Mösta, P.; Klion, H.; Schnetter, E. Neutrino-driven Turbulent Convection and Standing Accretion Shock Instability in Three-dimensional Core-collapse Supernovae. *Astrophys. J.* **2015**, *808*, 70, [[arXiv:astro-ph.HE/1409.7078](#)]. <https://doi.org/10.1088/0004-637X/808/1/70>.

29. Radice, D.; Ott, C.D.; Abdikamalov, E.; Couch, S.M.; Haas, R.; Schnetter, E. Neutrino-driven Convection in Core-collapse Supernovae: High-resolution Simulations. *Astrophys. J.* **2016**, *820*, 76, [[arXiv:astro-ph.HE/1510.05022](#)]. <https://doi.org/10.3847/0004-637X/820/1/76>.

30. Vartanyan, D.; Coleman, M.S.B.; Burrows, A. The collapse and three-dimensional explosion of three-dimensional massive-star supernova progenitor models. *MNRAS* **2022**, *510*, 4689–4705, [[arXiv:astro-ph.SR/2109.10920](#)]. <https://doi.org/10.1093/mnras/stab3702>.

31. Blondin, J.M.; Mezzacappa, A.; DeMarino, C. Stability of Standing Accretion Shocks, with an Eye toward Core-Collapse Supernovae. *Astrophys. J.* **2003**, *584*, 971–980, [[arXiv:astro-ph/astro-ph/0210634](#)]. <https://doi.org/10.1086/345812>.

32. Foglizzo, T.; Scheck, L.; Janka, H.T. Neutrino-driven Convection versus Advection in Core-Collapse Supernovae. *Astrophys. J.* **2006**, *652*, 1436–1450, [[arXiv:astro-ph/astro-ph/0507636](#)]. <https://doi.org/10.1086/508443>.

33. Müller, B.; Janka, H.T.; Heger, A. New Two-dimensional Models of Supernova Explosions by the Neutrino-heating Mechanism: Evidence for Different Instability Regimes in Collapsing Stellar Cores. *Astrophys. J.* **2012**, *761*, 72, [[arXiv:astro-ph.SR/1205.7078](#)]. <https://doi.org/10.1088/0004-637X/761/1/72>.

34. Couch, S.M.; Chatzopoulos, E.; Arnett, W.D.; Timmes, F.X. The Three-dimensional Evolution to Core Collapse of a Massive Star. *Astrophys. J. Lett.* **2015**, *808*, L21, [[arXiv:astro-ph.HE/1503.02199](#)]. <https://doi.org/10.1088/2041-8205/808/1/L21>.

35. Müller, B.; Melson, T.; Heger, A.; Janka, H.T. Supernova simulations from a 3D progenitor model - Impact of perturbations and evolution of explosion properties. *MNRAS* **2017**, *472*, 491–513, [[arXiv:astro-ph.SR/1705.00620](#)]. <https://doi.org/10.1093/mnras/stx1962>.

36. Kazeroni, R.; Abdikamalov, E. The impact of progenitor asymmetries on the neutrino-driven convection in core-collapse supernovae. *MNRAS* **2020**, *494*, 5360–5373, [[arXiv:astro-ph.SR/1911.08819](#)]. <https://doi.org/10.1093/mnras/staa944>.

37. Telman, Y.; Abdikamalov, E.; Foglizzo, T. Convective vortices in collapsing stars. *MNRAS* **2024**, *535*, 1388–1393, [[arXiv:astro-ph.SR/2409.17737](#)]. <https://doi.org/10.1093/mnras/stae2448>.

38. Heger, A.; Woosley, S.E.; Spruit, H.C. Presupernova Evolution of Differentially Rotating Massive Stars Including Magnetic Fields. *Astrophys. J.* **2005**, *626*, 350–363, [[arXiv:astro-ph/astro-ph/0409422](#)]. <https://doi.org/10.1086/429868>.

39. Popov, S.B.; Turolla, R. Initial spin periods of neutron stars in supernova remnants. *Astrophys. Space Sci.* **2012**, *341*, 457–464, [[arXiv:astro-ph.HE/1204.0632](#)]. <https://doi.org/10.1007/s10509-012-1100-z>.

40. Burrows, A.; Dessart, L.; Livne, E.; Ott, C.D.; Murphy, J. Simulations of Magnetically Driven Supernova and Hypernova Explosions in the Context of Rapid Rotation. *Astrophys. J.* **2007**, *664*, 416–434, [[astro-ph/0702539](#)]. <https://doi.org/10.1086/519161>.

41. Mösta, P.; Richers, S.; Ott, C.D.; Haas, R.; Piro, A.L.; Boydston, K.; Abdikamalov, E.; Reisswig, C.; Schnetter, E. Magnetorotational Core-collapse Supernovae in Three Dimensions. *Astrophys. J. Lett.* **2014**, *785*, L29, [[arXiv:astro-ph.HE/1403.1230](#)]. <https://doi.org/10.1088/2041-8205/785/2/L29>.

42. Kuroda, T.; Arcones, A.; Takiwaki, T.; Kotake, K. Magnetorotational Explosion of a Massive Star Supported by Neutrino Heating in General Relativistic Three-dimensional Simulations. *Astrophys. J.* **2020**, *896*, 102, [[arXiv:astro-ph.HE/2003.02004](#)]. <https://doi.org/10.3847/1538-4357/ab9308>.

43. Eisenberg, M.; Gottlieb, O.; Nakar, E. Observational signatures of stellar explosions driven by relativistic jets. *MNRAS* **2022**, *517*, 582–596, [[arXiv:astro-ph.HE/2201.08432](#)]. <https://doi.org/10.1093/mnras/stac2184>.

44. Pais, M.; Piran, T.; Nakar, E. The velocity distribution of outflows driven by choked jets in stellar envelopes. *MNRAS* **2023**, *519*, 1941–1954, [[arXiv:astro-ph.HE/2208.14459](#)]. <https://doi.org/10.1093/mnras/stac3640>.

45. Takiwaki, T.; Kotake, K.; Suwa, Y. Three-dimensional simulations of rapidly rotating core-collapse supernovae: finding a neutrino-powered explosion aided by non-axisymmetric flows. *MNRAS* **2016**, *461*, L112–L116, [[arXiv:astro-ph/1602.06759](https://arxiv.org/abs/astro-ph/1602.06759)]. <https://doi.org/10.1093/mnrasl/slw105>.

46. Summa, A.; Janka, H.T.; Melson, T.; Marek, A. Rotation-supported Neutrino-driven Supernova Explosions in Three Dimensions and the Critical Luminosity Condition. *Astrophys. J.* **2018**, *852*, 28, [[arXiv:astro-ph/1708.04154](https://arxiv.org/abs/astro-ph/1708.04154)]. <https://doi.org/10.3847/1538-4357/aa9ce8>.

47. Abdikamalov, E.; Foglizzo, T.; Mukazhanov, O. Impact of rotation on the evolution of convective vortices in collapsing stars. *MNRAS* **2021**, *503*, 3617–3628. <https://doi.org/10.1093/mnras/stab683>.

48. Buillet, A.C.; Foglizzo, T.; Guilet, J.; Abdikamalov, E. Effect of stellar rotation on the development of post-shock instabilities during core-collapse supernovae. *A&A* **2023**, *674*, A205, [[arXiv:astro-ph/2301.01962](https://arxiv.org/abs/astro-ph/2301.01962)]. <https://doi.org/10.1051/0004-6361/202245799>.

49. Powell, J.; Müller, B. The gravitational-wave emission from the explosion of a 15 solar mass star with rotation and magnetic fields. *MNRAS* **2024**, *532*, 4326–4339, [[arXiv:astro-ph/2406.09691](https://arxiv.org/abs/astro-ph/2406.09691)]. <https://doi.org/10.1093/mnras/stae1731>.

50. Torres-Forné, A.; Cerdá-Durán, P.; Obergaulinger, M.; Müller, B.; Font, J.A. Universal Relations for Gravitational-Wave Asteroseismology of Protoneutron Stars. *Phys. Rev. Lett.* **2019**, *123*, 051102, [[arXiv:gr-qc/1902.10048](https://arxiv.org/abs/gr-qc/1902.10048)]. <https://doi.org/10.1103/PhysRevLett.123.051102>.

51. Murphy, J.W.; Ott, C.D.; Burrows, A. A Model for Gravitational Wave Emission from Neutrino-Driven Core-Collapse Supernovae. *Astrophys. J.* **2009**, *707*, 1173–1190, [[arXiv:astro-ph/0907.4762](https://arxiv.org/abs/astro-ph/0907.4762)]. <https://doi.org/10.1088/0004-637X/707/2/1173>.

52. Morozova, V.; Radice, D.; Burrows, A.; Vartanyan, D. The Gravitational Wave Signal from Core-collapse Supernovae. *Astrophys. J.* **2018**, *861*, 10, [[arXiv:astro-ph/1801.01914](https://arxiv.org/abs/astro-ph/1801.01914)]. <https://doi.org/10.3847/1538-4357/aac5f1>.

53. Ott, C.D.; Abdikamalov, E.; Mösta, P.; Haas, R.; Drasco, S.; O'Connor, E.P.; Reisswig, C.; Meakin, C.A.; Schnetter, E. General-relativistic Simulations of Three-dimensional Core-collapse Supernovae. *Astrophys. J.* **2013**, *768*, 115, [[arXiv:astro-ph/1210.6674](https://arxiv.org/abs/astro-ph/1210.6674)]. <https://doi.org/10.1088/0004-637X/768/2/115>.

54. Yakunin, K.N.; Mezzacappa, A.; Marronetti, P.; Yoshida, S.; Bruenn, S.W.; Hix, W.R.; Lentz, E.J.; Bronson Messer, O.E.; Harris, J.A.; Endeve, E.; et al. Gravitational wave signatures of ab initio two-dimensional core collapse supernova explosion models for 12–25 M_{\odot} stars. *Phys. Rev. D* **2015**, *92*, 084040, [[arXiv:astro-ph/1505.05824](https://arxiv.org/abs/astro-ph/1505.05824)]. <https://doi.org/10.1103/PhysRevD.92.084040>.

55. Kuroda, T.; Kotake, K.; Takiwaki, T. A New Gravitational-wave Signature from Standing Accretion Shock Instability in Supernovae. *Astrophys. J. Lett.* **2016**, *829*, L14, [[arXiv:astro-ph/1605.09215](https://arxiv.org/abs/astro-ph/1605.09215)]. <https://doi.org/10.3847/2041-8205/829/1/L14>.

56. Mezzacappa, A.; Marronetti, P.; Landfield, R.E.; Lentz, E.J.; Murphy, R.D.; Raphael Hix, W.; Harris, J.A.; Bruenn, S.W.; Blondin, J.M.; Bronson Messer, O.E.; et al. Core collapse supernova gravitational wave emission for progenitors of 9.6, 15, and 25 M_{\odot} . *Phys. Rev. D* **2023**, *107*, 043008, [[arXiv:astro-ph/2208.10643](https://arxiv.org/abs/astro-ph/2208.10643)]. <https://doi.org/10.1103/PhysRevD.107.043008>.

57. Vartanyan, D.; Burrows, A.; Wang, T.; Coleman, M.S.B.; White, C.J. Gravitational-wave signature of core-collapse supernovae. *Phys. Rev. D* **2023**, *107*, 103015, [[arXiv:astro-ph/2302.07092](https://arxiv.org/abs/astro-ph/2302.07092)]. <https://doi.org/10.1103/PhysRevD.107.103015>.

58. Mueller, E.; Janka, H.T. Gravitational radiation from convective instabilities in Type II supernova explosions. *A&A* **1997**, *317*, 140–163.

59. Choi, L.; Burrows, A.; Vartanyan, D. Gravitational-wave and Gravitational-wave Memory Signatures of Core-collapse Supernovae. *Astrophys. J.* **2024**, *975*, 12, [[arXiv:astro-ph/2408.01525](https://arxiv.org/abs/astro-ph/2408.01525)]. <https://doi.org/10.3847/1538-4357/ad74f8>.

60. Müller, E.; Janka, H.T.; Wongwathanarat, A. Parametrized 3D models of neutrino-driven supernova explosions. Neutrino emission asymmetries and gravitational-wave signals. *A&A* **2012**, *537*, A63, [[arXiv:astro-ph/1106.6301](https://arxiv.org/abs/astro-ph/1106.6301)]. <https://doi.org/10.1051/0004-6361/201117611>.

61. Birnholz, O.; Piran, T. Gravitational wave memory from gamma ray bursts' jets. *Phys. Rev. D* **2013**, *87*, 123007, [[arXiv:astro-ph/1302.5713](https://arxiv.org/abs/astro-ph/1302.5713)]. <https://doi.org/10.1103/PhysRevD.87.123007>.

62. Gottlieb, O.; Nagakura, H.; Tchekhovskoy, A.; Natarajan, P.; Ramirez-Ruiz, E.; Banagiri, S.; Jacquemin-Ide, J.; Kaaz, N.; Kalogera, V. Jetted and Turbulent Stellar Deaths: New LVK-detectable Gravitational-wave Sources. *Astrophys. J. Lett.* **2023**, *951*, L30, [[arXiv:astro-ph/2209.09256](https://arxiv.org/abs/astro-ph/2209.09256)]. <https://doi.org/10.3847/2041-8213/ace03a>.

63. Soker, N. Predicting Gravitational Waves from Jittering-jets-driven Core Collapse Supernovae. *Research in Astronomy and Astrophysics* **2023**, *23*, 121001, [[arXiv:astro-ph/2308.04329](https://arxiv.org/abs/astro-ph/2308.04329)]. <https://doi.org/10.1088/1674-4527/ad013e>.

64. Ott, C.D.; Abdikamalov, E.; O'Connor, E.; Reisswig, C.; Haas, R.; Kalmus, P.; Drasco, S.; Burrows, A.; Schnetter, E. Correlated gravitational wave and neutrino signals from general-relativistic rapidly rotating iron core collapse. *Phys. Rev. D* **2012**, *86*, 024026, [[arXiv:astro-ph/1204.0512](https://arxiv.org/abs/astro-ph/1204.0512)]. <https://doi.org/10.1103/PhysRevD.86.024026>.

65. Fuller, J.; Klion, H.; Abdikamalov, E.; Ott, C.D. Supernova seismology: gravitational wave signatures of rapidly rotating core collapse. *MNRAS* **2015**, *450*, 414–427, [[arXiv:astro-ph/1501.06951](https://arxiv.org/abs/astro-ph/1501.06951)]. <https://doi.org/10.1093/mnras/stv698>.

66. Scheidegger, S.; Fischer, T.; Whitehouse, S.C.; Liebendörfer, M. Gravitational waves from 3D MHD core collapse simulations. *A&A* **2008**, *490*, 231–241, [[arXiv:astro-ph/0709.0168](https://arxiv.org/abs/astro-ph/0709.0168)]. <https://doi.org/10.1051/0004-6361:20078577>.

67. Shibagaki, S.; Kuroda, T.; Kotake, K.; Takiwaki, T. A new gravitational-wave signature of low-T/|W| instability in rapidly rotating stellar core collapse. *MNRAS* **2020**, *493*, L138–L142, [[arXiv:astro-ph/1909.09730](https://arxiv.org/abs/astro-ph/1909.09730)]. <https://doi.org/10.1093/mnrasl/slaa021>.

68. Nunes, S.; Escrig, G.; Freitas, O.G.; Font, J.A.; Fernandes, T.; Onofre, A.; Torres-Forné, A. Deep-learning classification and parameter inference of rotational core-collapse supernovae. *Phys. Rev. D* **2024**, *110*, 064037, [[arXiv:astro-ph/2403.04938](https://arxiv.org/abs/astro-ph/2403.04938)]. <https://doi.org/10.1103/PhysRevD.110.064037>.

69. Pastor-Marcos, C.; Cerdá-Durán, P.; Walker, D.; Torres-Forné, A.; Abdikamalov, E.; Richers, S.; Font, J.A. Bayesian inference from gravitational waves in fast-rotating, core-collapse supernovae. *Phys. Rev. D* **2024**, *109*, 063028, [[arXiv:astro-ph/2308.03456](https://arxiv.org/abs/astro-ph/2308.03456)]. <https://doi.org/10.1103/PhysRevD.109.063028>.

70. Villegas, L.O.; Moreno, C.; Pajkos, M.A.; Zanolini, M.; Antelis, J.M. Parameter estimation from the core-bounce phase of rotating core collapse supernovae in real interferometer noise. *Classical and Quantum Gravity* **2025**, *42*, 115001. <https://doi.org/10.1088/1361-6382/add235>.

71. Abdikamalov, E.; Gossan, S.; DeMaio, A.M.; Ott, C.D. Measuring the angular momentum distribution in core-collapse supernova progenitors with gravitational waves. *Phys. Rev. D* **2014**, *90*, 044001, [[arXiv:astro-ph/1311.3678](https://arxiv.org/abs/astro-ph/1311.3678)]. <https://doi.org/10.1103/PhysRevD.90.044001>.

72. Bizouard, M.A.; Maturana-Russel, P.; Torres-Forné, A.; Obergaulinger, M.; Cerdá-Durán, P.; Christensen, N.; Font, J.A.; Meyer, R. Inference of protoneutron star properties from gravitational-wave data in core-collapse supernovae. *Phys. Rev. D* **2021**, *103*, 063006, [[arXiv:gr-qc/2012.00846](https://arxiv.org/abs/gr-qc/2012.00846)]. <https://doi.org/10.1103/PhysRevD.103.063006>.

73. Bruel, T.; Bizouard, M.A.; Obergaulinger, M.; Maturana-Russel, P.; Torres-Forné, A.; Cerdá-Durán, P.; Christensen, N.; Font, J.A.; Meyer, R. Inference of protoneutron star properties in core-collapse supernovae from a gravitational-wave detector network. *Phys. Rev. D* **2023**, *107*, 083029, [[arXiv:astro-ph/2301.10019](https://arxiv.org/abs/astro-ph/2301.10019)]. <https://doi.org/10.1103/PhysRevD.107.083029>.

74. Casallas-Lagos, A.; Antelis, J.M.; Moreno, C.; Zanolini, M.; Mezzacappa, A.; Szczepańczyk, M.J. Characterizing the temporal evolution of the high-frequency gravitational wave emission for a core collapse supernova with laser interferometric data: A neural network approach. *Phys. Rev. D* **2023**, *108*, 084027. <https://doi.org/10.1103/PhysRevD.108.084027>.

75. Logue, J.; Ott, C.D.; Heng, I.S.; Kalmus, P.; Scargill, J.H.C. Inferring core-collapse supernova physics with gravitational waves. *Phys. Rev. D* **2012**, *86*, 044023, [[arXiv:gr-qc/1202.3256](https://arxiv.org/abs/gr-qc/1202.3256)]. <https://doi.org/10.1103/PhysRevD.86.044023>.

76. Powell, J.; Iess, A.; Llorens-Monteagudo, M.; Obergaulinger, M.; Müller, B.; Torres-Forné, A.; Cuoco, E.; Font, J.A. Determining the core-collapse supernova explosion mechanism with current and future gravitational-wave observatories. *Phys. Rev. D* **2024**, *109*, 063019, [[arXiv:astro-ph/2311.18221](https://arxiv.org/abs/astro-ph/2311.18221)]. <https://doi.org/10.1103/PhysRevD.109.063019>.

77. Richers, S.; Ott, C.D.; Abdikamalov, E.; O'Connor, E.; Sullivan, C. Equation of state effects on gravitational waves from rotating core collapse. *Phys. Rev. D* **2017**, *95*, 063019, [[arXiv:astro-ph/1701.02752](https://arxiv.org/abs/astro-ph/1701.02752)]. <https://doi.org/10.1103/PhysRevD.95.063019>.

78. Edwards, M.C. Classifying the equation of state from rotating core collapse gravitational waves with deep learning. *Phys. Rev. D* **2021**, *103*, 024025, [[arXiv:astro-ph/2009.07367](https://arxiv.org/abs/astro-ph/2009.07367)]. <https://doi.org/10.1103/PhysRevD.103.024025>.

79. Chao, Y.S.; Su, C.Z.; Chen, T.Y.; Wang, D.W.; Pan, K.C. Determining the Core Structure and Nuclear Equation of State of Rotating Core-collapse Supernovae with Gravitational Waves by Convolutional Neural Networks. *Astrophys. J.* **2022**, *939*, 13, [[arXiv:astro-ph/2209.10089](https://arxiv.org/abs/astro-ph/2209.10089)]. <https://doi.org/10.3847/1538-4357/ac930e>.

80. Wolfe, N.E.; Fröhlich, C.; Miller, J.M.; Torres-Forné, A.; Cerdá-Durán, P. Gravitational Wave Eigenfrequencies from Neutrino-driven Core-collapse Supernovae. *Astrophys. J.* **2023**, *954*, 161, [[arXiv:astro-ph/2303.16962](https://arxiv.org/abs/astro-ph/2303.16962)]. <https://doi.org/10.3847/1538-4357/ace693>.

81. Murphy, R.D.; Casallas-Lagos, A.; Mezzacappa, A.; Zanolini, M.; Landfield, R.E.; Lentz, E.J.; Marronetti, P.; Antelis, J.M.; Moreno, C. Dependence of the reconstructed core-collapse supernova gravitational wave high-frequency feature on the nuclear equation of state in real interferometric data. *Phys. Rev. D* **2024**, *110*, 083006, [[arXiv:astro-ph/2406.01784](https://arxiv.org/abs/astro-ph/2406.01784)]. <https://doi.org/10.1103/PhysRevD.110.083006>.

82. Abylkairov, Y.S.; Edwards, M.C.; Orel, D.; Mitra, A.; Shukirgaliyev, B.; Abdikamalov, E. Evaluating machine learning models for supernova gravitational wave signal classification. *Machine Learning: Science and Technology* **2024**, *5*, 045077, [[arXiv:astro-ph/2409.14508](https://arxiv.org/abs/astro-ph/2409.14508)]. <https://doi.org/10.1088/2632-2153/ada33a>.

83. Abylkairov, Y.S.; Edwards, M.C.; Ostrikov, A.; Tleukhanov, Y.; Torres-Forné, A.; Cerdá-Durán, P.; Font, J.A.; Szczepańczyk, M.J.; Abdikamalov, E. Assessing the Distance for Probing the Nuclear Equation of State with Supernova Gravitational Waves. *arXiv preprint arXiv:2510.15102* **2025**.

84. Pajkos, M.A.; Couch, S.M.; Pan, K.C.; O'Connor, E.P. Features of Accretion-phase Gravitational-wave Emission from Two-dimensional Rotating Core-collapse Supernovae. *Astrophys. J.* **2019**, *878*, 13, [[arXiv:astro-ph/1901.09055](https://arxiv.org/abs/astro-ph/1901.09055)]. <https://doi.org/10.3847/1538-4357/ab1de2>.

85. Pajkos, M.A.; Warren, M.L.; Couch, S.M.; O'Connor, E.P.; Pan, K.C. Determining the Structure of Rotating Massive Stellar Cores with Gravitational Waves. *Astrophys. J.* **2021**, *914*, 80, [[arXiv:astro-ph/2011.09000](https://arxiv.org/abs/astro-ph/2011.09000)]. <https://doi.org/10.3847/1538-4357/abfb65>.

86. Mitra, A.; Orel, D.; Abylkairov, Y.S.; Shukirgaliyev, B.; Abdikamalov, E. Probing nuclear physics with supernova gravitational waves and machine learning. *MNRAS* **2024**, *529*, 3582–3592, [[arXiv:astro-ph/2310.15649](https://arxiv.org/abs/astro-ph/2310.15649)]. <https://doi.org/10.1093/mnras/stae714>.

87. Gossan, S.E.; Sutton, P.; Stuver, A.; Zanolin, M.; Gill, K.; Ott, C.D. Observing gravitational waves from core-collapse supernovae in the advanced detector era. *Phys. Rev. D* **2016**, *93*, 042002, [[arXiv:astro-ph.HE/1511.02836](https://arxiv.org/abs/1511.02836)]. <https://doi.org/10.1103/PhysRevD.93.042002>.

88. Szczepański, M.J.; Antelis, J.M.; Benjamin, M.; Cavaglià, M.; Gondek-Rosińska, D.; Hansen, T.; Klimenko, S.; Morales, M.D.; Moreno, C.; Mukherjee, S.; et al. Detecting and reconstructing gravitational waves from the next galactic core-collapse supernova in the advanced detector era. *Phys. Rev. D* **2021**, *104*, 102002, [[arXiv:astro-ph.HE/2104.06462](https://arxiv.org/abs/2104.06462)]. <https://doi.org/10.1103/PhysRevD.104.102002>.

89. Gabor, D. Theory of communication. Part 1: The analysis of information. *Journal of the Institution of Electrical Engineers - Part III: Radio and Communication Engineering* **1946**, *93*, 429–441. <https://doi.org/10.1049/jiee.1946.0050>.

90. Allen, J.B.; Rabiner, L.R. A unified approach to short-time Fourier analysis and synthesis. *Proceedings of the IEEE* **2005**, *65*, 1558–1564. <https://doi.org/10.1109/PROC.1977.10705>.

91. Guo, T.; et al. A review of wavelet analysis and its applications: Challenges and opportunities. *IEEE Access* **2022**, *10*, 58869–58903. <https://doi.org/10.1109/ACCESS.2022.3186351>.

92. Stepanov, R.; et al. Wavelet analysis of the long-term activity of V833 Tau. *MNRAS* **2020**, *495*, 3788–3794. <https://doi.org/10.1093/mnras/staa1444>.

93. Shannon, C.E. A mathematical theory of communication. *The Bell system technical journal* **1948**, *27*, 379–423. <https://doi.org/10.1002/j.1538-7305.1948.tb01338.x>.

94. Pal, N.R.; Pal, S.K. Entropy: A new definition and its applications. *IEEE transactions on systems, man, and cybernetics* **2002**, *21*, 1260–1270. <https://doi.org/10.1109/21.120079>.

95. Tsallis, C. Possible generalization of Boltzmann-Gibbs statistics. *Journal of statistical physics* **1988**, *52*, 479–487. <https://doi.org/10.1007/BF01016429>.

96. Rényi, A.; et al. On measures of information and entropy. In Proceedings of the Proceedings of the 4th Berkeley symposium on mathematics, statistics and probability, 1961, Vol. 1.

97. Li, J.; et al. Feature selection: A data perspective. *ACM Computing Surveys (CSUR)* **2017**, *50*, 1–45. <https://doi.org/10.1145/3136625>.

98. Venkatesh, B.; Anuradha, J. A review of feature selection and its methods. *Cybern. Inf. Technol.* **2019**, *19*, 3–26. <https://doi.org/10.2478/cait-2019-0001>.

99. Muthukrishnan, R.; Rohini, R. LASSO: A feature selection technique in predictive modeling for machine learning. In Proceedings of the 2016 IEEE International Conference on Advances in Computer Applications (ICACA). IEEE, 2016, pp. 18–20. <https://doi.org/10.1109/ICACA.2016.7887916>.

100. Saiz-Pérez, A.; Torres-Forné, A.; Font, J.A. Classification of core-collapse supernova explosions with learned dictionaries. *MNRAS* **2022**, *512*, 3815–3827, [[arXiv:gr-qc/2110.12941](https://arxiv.org/abs/2110.12941)]. <https://doi.org/10.1093/mnras/stac698>.

101. Powell, J.; Iess, A.; Llorens-Monteagudo, M.; Obergaulinger, M.; Müller, B.; Torres-Forné, A.; Cuoco, E.; Font, J.A. Determining the core-collapse supernova explosion mechanism with current and future gravitational-wave observatories. *Phys. Rev. D* **2024**, *109*, 063019, [[arXiv:astro-ph.HE/2311.18221](https://arxiv.org/abs/2311.18221)]. <https://doi.org/10.1103/PhysRevD.109.063019>.

102. Awad, M.; Fraihat, S. Recursive feature elimination with cross-validation with decision tree: Feature selection method for machine learning-based intrusion detection systems. *Journal of Sensor and Actuator Networks* **2023**, *12*, 67. <https://doi.org/10.3390/jsan12050067>.

103. Urbanowicz, R.J.; et al. Relief-based feature selection: Introduction and review. *Journal of Biomedical Informatics* **2018**, *85*, 189–203. <https://doi.org/10.1016/j.jbi.2018.07.014>.

104. Huang, Z.; et al. A hybrid feature selection method based on binary state transition algorithm and ReliefF. *IEEE Journal of Biomedical and Health Informatics* **2018**, *23*, 1888–1898. <https://doi.org/10.1109/JBHI.2018.2819799>.

105. Pedregosa, F.; Varoquaux, G.; Gramfort, A.; Michel, V.; Thirion, B.; Grisel, O.; Blondel, M.; Prettenhofer, P.; Weiss, R.; Dubourg, V.; et al. Scikit-learn: Machine learning in Python. *the Journal of machine Learning research* **2011**, *12*, 2825–2830.

106. Dimmelmeier, H.; Font, J.A.; Müller, E. Relativistic simulations of rotational core collapse I. Methods, initial models, and code tests. *A&A* **2002**, *388*, 917–935, [[arXiv:astro-ph/0204288](https://arxiv.org/abs/astro-ph/0204288)]. <https://doi.org/10.1051/0004-6361:20020563>.

107. Dimmelmeier, H.; Novak, J.; Font, J.A.; Ibáñez, J.M.; Müller, E. Combining spectral and shock-capturing methods: A new numerical approach for 3D relativistic core collapse simulations **2005**, *71*, 064023, [[astro-ph/0407174](https://arxiv.org/abs/astro-ph/0407174)]. <https://doi.org/10.1103/PhysRevD.71.064023>.

108. Woosley, S.E.; Heger, A. Nucleosynthesis and remnants in massive stars of solar metallicity. *Physics Reports* **2007**, *442*, 269, [[arXiv:astro-ph/0702176](https://arxiv.org/abs/astro-ph/0702176)].

109. Woosley, S.E.; Heger, A.; Weaver, T.A. The evolution and explosion of massive stars. *Rev. Mod. Phys.* **2002**, *74*, 1015.

110. Flanagan, E.E.; Hughes, S.A. Measuring gravitational waves from binary black hole coalescences. I. Signal to noise for inspiral, merger, and ringdown. *Phys. Rev. D* **1998**, *57*, 4535–4565. <https://doi.org/10.1103/PhysRevD.57.4535>.

111. Inouye, T.; Shinosaki, K.; Sakamoto, H.; Toi, S.; Ukai, S.; Iyama, A.; Katsuda, Y.; Hirano, M. Quantification of EEG irregularity by use of the entropy of the power spectrum. *Electroencephalography and Clinical Neurophysiology* **1991**, *79*, 204–210. [https://doi.org/10.1016/0013-4694\(91\)90138-t](https://doi.org/10.1016/0013-4694(91)90138-t).
112. Toh, A.M.; Tognoni, R.; Nordholm, S. Spectral entropy as speech features for speech recognition. In Proceedings of the Proceedings of PEECS, 2005, Vol. 1, p. 92.
113. Tenev, A.; et al. Entropy, complexity, and spectral features of EEG signals in autism and typical development: a quantitative approach. *Frontiers in Psychiatry* **2025**, *16*, 1505297. <https://doi.org/https://doi.org/10.3389/fpsyg.2025.1505297>.